https://doi.org/10.1016/j.engstruct.2019.05.026

Efficient calculation and monitoring of temperature actions on supertall structures

Fei Gao[1], Pan Chen[2], Yong Xia[3*], Hong-Ping Zhu[4] and Shun Weng[5]

Abstract: Numerical heat transfer analysis and field monitoring have been developed to investigate the effects of varying temperature on supertall buildings. The conventional heat transfer analysis studies one or several components of a structure each time, causing the calculated temperature of the entire structure inaccurate. Moreover, the finite element (FE) model used for calculating temperature distribution cannot be directly used for computing the temperature-induced responses of the structure, which requires considerable manual inputs of the temperature load. This paper presents an automatic and efficient FE approach to calculating the temperature distribution and the associated responses of an entire structure using field meteorological monitoring data. The position of the sun relative to the structure can be determined by introducing a new radiation calendar timing system. A virtual sun is then created to determine the irradiation and shade elements of the structural model, from which the solar radiation intensity on the surfaces of all elements can be calculated at any particular time on any particular day. Consequently, the dynamic thermal boundary conditions of the FE model are formulated automatically. This enables the heat transfer analysis of the entire structure to be conducted and the temperature distribution of the entire structure to be calculated in real time. The calculated temperature distribution is transferred to the temperature load in the same FE model, and the temperature-induced

1 Professor, School of Civil Engineering and Mechanics, Huazhong University of Science and Technology, Wuhan, Hubei, PR China.
2 PhD Student, School of Civil Engineering and Mechanics, Huazhong University of Science and Technology, Wuhan, Hubei, PR China.
3 Professor, Department of Civil and Environment Engineering, The Hong Kong Polytechnic University, Hong Kong, PR China (Corresponding author). E-mail: ceyxia@polyu.edu.hk
4 Professor, School of Civil Engineering and Mechanics, Huazhong University of Science and Technology, Wuhan, Hubei, PR China.
5 Professor, School of Civil Engineering and Mechanics, Huazhong University of Science and Technology, Wuhan, Hubei, PR China.

stress and displacement responses of the structure can be obtained. The method is applied to the 335 m tall Wuhan Yangtze River Navigation Centre. A 3D solid FE model of this structure during the construction stage is established. Varying wind speed and air temperature along the height of the structure are taken into account from the SHM system. The calculated temperature distribution and temperature-induced stress of the structure are in good agreement with the field monitoring data. The proposed technique offers an effective and efficient real-time monitoring of the temperature actions on large-scale structures.

Keywords: Supertall structures; field monitoring; temperature action; heat transfer analysis

1. Introduction

An increasing number of supertall buildings are being constructed worldwide. During the long construction period, a supertall building which has an incomplete structural system is vulnerable to the changing environment. The solar radiation causes a nonuniform temperature distribution of the structure, thereby leading to changes in the structural stresses and displacement, which may be at a similar level as those by typhoons [1].

Most investigations of the structural temperature effect focus on bridges. The thermal load [2], temperature distribution [3–5] and temperature-induced responses [6–9] of bridge structures have been studied extensively. Configuration of a bridge is relatively simple, for example, a cross section of a bridge can be a girder or box. However, a cross section of a supertall structure may consist of a quite number of columns, beams and walls and each surface may receive different solar radiation, causing the temperature distribution very complicated. So far research of the temperature effects on supertall buildings is limited and most of past studies focus on tower-type structures. For example, Pirner et al. [10] recorded a two-day stress cycle of a TV tower caused by temperature changes and found that the stresses decreased in the morning and increased in the afternoon. Tamura et al. [11] measured the static displacement of a 108 m-high steel tower caused by temperature variations. The top of the tower moved by approximately 4 cm northwest after sunrise and gradually returned to the initial point after sunset. The trajectory of the top was nearly circular in shape in one daytime. Breuer et al. [12] monitored the horizontal displacements of the top of the Stuttgart TV tower caused by the combined influence of solar radiation and daily air temperature variation during a sunny summer day. The daily moving trajectory varied daily and was related to the ambient air temperature and sunshine duration. Xia et al. [13] used real-time strain data to calculate the temperature- and wind-induced deformation of the 600 m-tall Canton Tower based on the long-term structural health monitoring (SHM) system. Su et al. [14] found that the maximum horizontal displacement of the Canton Tower caused by temperature change could reach approximately 20 cm in one day. The temperature-induced stress variation in different seasons could reach 25% of the total stress for the inner tube and 11% for the outer tube. Hu et al. [15] employed multiple linear regressions to investigate the temperature-induced displacement of the Canton Tower, from which the temperature- and wind-induced displacements of the structure could be separated.

In practice, SHM systems always have a limited number of sensors, and the numerical analysis may provide detailed information that is unavailable from the SHM systems. In the conventional numerical analysis, the bridge components, such as the deck and towers, are separately modeled with a two-dimensional (2D) or three-dimensional (3D) model by ignoring the temperature variation in the longitudinal direction of the component. The temperature distributions of the components are subsequently obtained from the local transient analysis and then assembled and input into a global finite element (FE) model of the entire bridge to calculate the temperature-induced responses via a structural analysis [16-18]. However, such divide-and-conquer approach is inaccurate and inefficient for thermal analysis of supertall structures for following reasons. First, a supertall structure is typically composed of a large number of continuous components. The temperature distribution at the interface of components will be discontinuous if each component is analysed separately. Second, the temperature distribution of the supertall structure along the height is not uniform. Su et al. [14] found that the average decrease rate of air temperature is approximately 6.7 °C/km as altitude increases. This indicates that the vertical thermal boundary conditions of a supertall structure are different. Third, the conventional process requires considerable manual intervention by inputting the temperature loads to the 3D FE model. This drawback causes the temperature behavior analysis to be performed at several particular time instants only, neither in real-time nor continuously [19].

This paper presents an automatic FE analytical method for fast calculation of the temperature distribution and temperature-induced responses of an entire supertall structure for the first time. The technique is applied to a 335 m tall supertall structure under construction, on which a long-term SHM system has been installed. A 3D global FE model of the supertall structure is established and automatic heat-transfer analysis is conducted. The calculated temperature distribution is then inputted to the same FE model while with different type of elements. The temperature-induced stresses and horizontal displacement are obtained with a structural analysis.

2. Global heat transfer analysis of a building structure

2.1. Determination of the relative position of the sun

The relative position of the sun varies in a yearly period. The sun position relative to any object on the ground can be determined by three parameters, namely, solar altitude angle β, solar azimuth angle α and the distance of the sun from the earth d, as shown in Fig. 1. The distance d is usually treated as a constant. α and β are related to latitude φ, solar hour angle ω and solar declination δ as follows [20]:

$$\sin\beta = \sin\varphi\sin\delta + \cos\varphi\cos\delta\cos\omega, \tag{1}$$

$$\sin\alpha = \frac{\cos\delta\sin\omega}{\cos\beta}, \qquad \cos\alpha = \frac{\sin\beta\sin\varphi - \sin\delta}{\cos\beta\cos\varphi}. \tag{2}$$

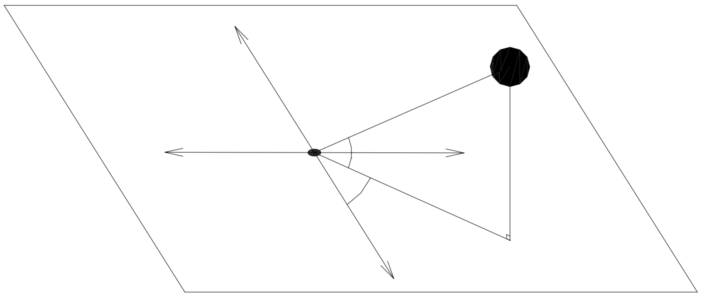

Fig. 1. Relative position of the sun and object on the gound

The solar declination, the angle between the equatorial plane and the sun–earth centreline (Fig. 2(a)), changes with the revolution of the earth around the sun. During one year, the solar declination changes with the following routine: 0° (vernal equinox) → 23.5° (summer solstice) → 0° (autumnal equinox) → −23.5° (winter solstice) → 0° (vernal equinox). This routine can be regarded as a sinusoidal function between −23.5° and +23.5° in one year.

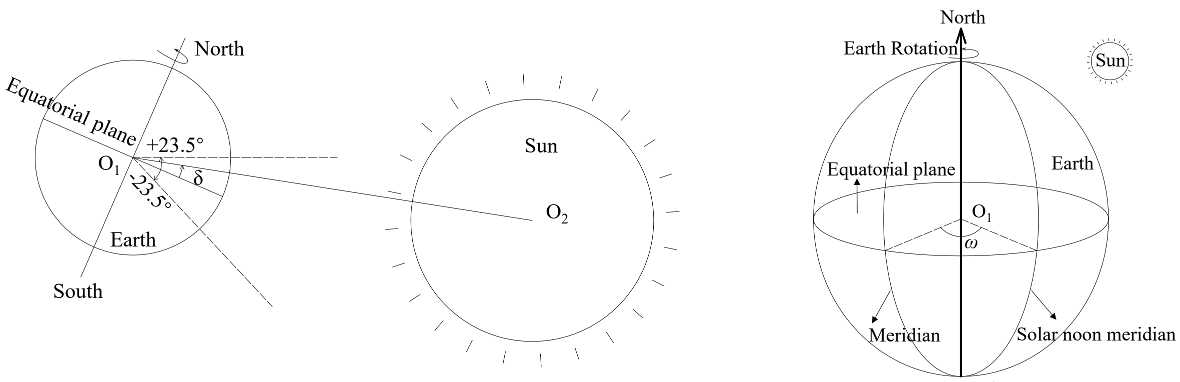

(a) Solar declination δ

(b) Solar hour angle ω

Fig. 2. Solar declination and solar hour angle

The solar hour angle, the angle between the solar noon meridian and the meridian (Fig. 2(b)), changes with the earth's rotation. In one day, the solar hour angle ranges from 0° to 360° and changes by 15° per hour. A new timing system, namely, the radiation calendar system [21], is used in this study to unify the time parameter of the solar declination and the solar hour angle. In the system, the solar hour angle is accumulated every day and thus has a period of one year. The updated solar hour angle is called the radiation calendar angle τ.

In the radiation calendar system, March 21 (vernal equinox) 0:00:00 is set as the reference. The radiation calendar angle τ increases by 15° per hour and changes from 0° to 131,400° (= 15 × 24 × 365) per year. τ is unique and corresponds to a specified date in one year. If the specified date is given in the form of *Year*/*Month*/*Day* and *Hour*/*Min*/*Sec*, then τ can be expressed as follows:

$$\tau = 360 \times D + 15 \times Hour + \frac{Min}{4} + \frac{Sec}{240}, \tag{3}$$

where D indicates the number of days relative to the reference, March 21. For example, at 6:30:00 of March 22, τ can be calculated as follows:

$$\tau = 360 \times 1 + 15 \times 6 + \frac{1}{4} \cdot 30 + \frac{1}{240} \cdot 0 = 457.5^\circ . \tag{4}$$

With the radiation calendar angle τ, the solar declination δ can be expressed by

$$\delta = 23.5 \sin(\frac{\tau}{365}) . \tag{5}$$

The relationship between the radiation calendar angle τ and the solar hour angle ω is as follows:

$$\tau = 360 \cdot D + \omega . \tag{6}$$

Eqs. (5) and (6) are substituted into Eqs. (1) and (2), and the solar altitude and solar azimuth angles can be rewritten as the following equations, where only two variable parameters (φ and τ) are required:

$$\beta = \arcsin\left\{ \sin\varphi \sin[23.5\sin(\frac{\tau}{365})] + \cos\varphi \cos[23.5\sin(\frac{\tau}{365})]\cos\tau \right\}, \tag{7}$$

$$\alpha = \begin{cases} 360 - \arccos\left\{ \dfrac{\sin\beta\sin\varphi - \sin[23.5\sin(\frac{\tau}{365})]}{\cos\beta\cos\varphi} \right\}, 360m < \tau \le 360m + 180 \\ \arccos\left\{ \dfrac{\sin\beta\sin\varphi - \sin[23.5\sin(\frac{\tau}{365})]}{\cos\beta\cos\varphi} \right\}, 360m + 180 < \tau \le 360m + 360 \end{cases}, \tag{8}$$

where m = 0, 1, 2, … , 364.

2.2. Hemicube method

The most difficult and challenging part of the thermal analysis lies in the means of applying the real solar radiation intensity to the FE model because a structure consists of a large number of elements and the irradiation and shade faces of the elements change continuously with the rotation of the sun. In this study, the irradiation and shade faces are determined by the hemicube method [22]. This method is originally used to calculate the angle coefficient, which is a radiation energy percentage that is emitted from a surface to another. The propagation of sunlight is also a type of radiant energy transmission. Therefore, the irradiation and shade faces formed by the projection of sunlight onto a structure surface can be determined by the hemicube method.

A hemicube that is 1 m long, 1 m wide and 0.5 m high is regarded as an example. The radiation element (S) is located at the bottom centre of the hemicube, as shown in Fig. 3. The angle coefficient between the radiation element (S) and absorption element (A1) is equal to the area (A0) mapped on the hemicube when the line (Line 1) between the radiation and absorption elements crosses through the hemicube only. However, the angle coefficient is equal to 0 when the line crosses through not only the hemicube but also other areas, such as Line 2. Consequently, if the angle coefficient is not equal to zero, then the radiation element can ‘see’ the absorption element, which is defined as the irradiation element. Otherwise, the radiation element that cannot ‘see’ the absorption element is the shade element. The value of the angle coefficient is used to distinguish the shade and irradiation elements automatically.

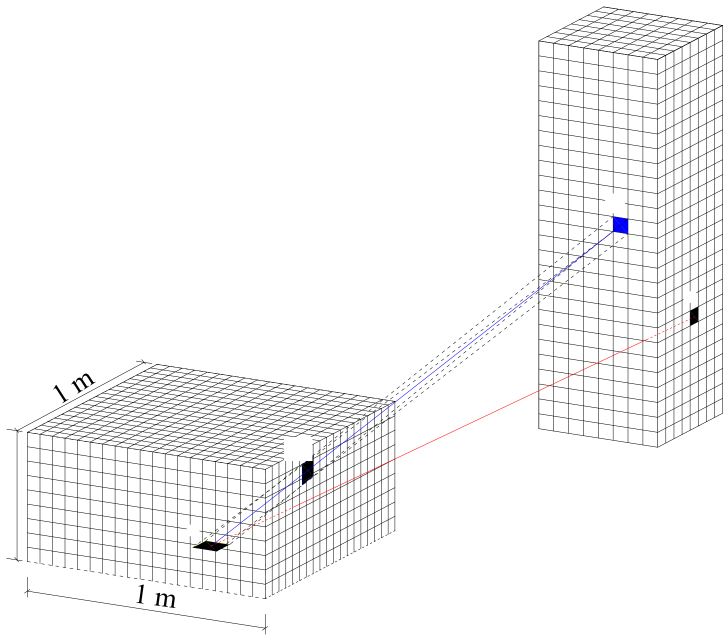

Fig. 3. Hemicube method

2.3. Heat transfer equations and boundary conditions

The temperature distribution T of a structure at time t can be expressed by the well-known Fourier heat conduction equation as follows:

$$\rho c \frac{\partial T}{\partial t} = k_x \frac{\partial^2 T}{\partial x^2} + k_y \frac{\partial^2 T}{\partial y^2} + k_z \frac{\partial^2 T}{\partial z^2}, \tag{9}$$

where x, y and z are Cartesian coordinates; ρ (kg/m^3) represents the density of the material; c (J/(kg·°C)) is the specific heat coefficient; T (°C) is the structure temperature at coordinate point (x, y, z); and k_x, k_y and k_z (W/(m·°C)) represent the thermal conductivity coefficients of different directions. The Fourier heat conduction equation establishes the relationship among temperature, time and space. The thermal initial and boundary conditions are required for solving Eq. (9). A boundary condition that considers not only solar radiation but also environment temperature is used here, and the formula can be expressed as follows [23]:

$$(h_c + h_r)(T_a + \frac{\alpha_s I}{h_c + h_r} - T) + k \frac{\partial T}{\partial n} = 0, \tag{10}$$

$$h_c + h_r = 9.8 + 3.8v, \tag{11}$$

where h_c (W/(m^2·°C)) represents the convection coefficient between the surfaces and the ambient air; h_r (W/(m^2·°C)) is the radiant heat transfer coefficient; h_c and h_r are in correlation with mean wind speed v, which is simplified as Eq. (11) on the basis of empirical formulae [3]; T_a (°C) represents the environmental air temperature; α_s ($0 < \alpha_s < 1$) is the absorptivity coefficient of the surface; I (W/m^2) is the intensity of solar radiation projected onto the surface; k (W/(m·°C)) represents the thermal conductivity coefficient of the material and is assumed identical in three directions; n is the normal direction of the surface.

A real supertall structure is used to demonstrate the procedures of calculating the thermal distribution of the entire structure.

3. Wuhan Yangtze River Navigation Centre and its SHM system

3.1. Description of Wuhan Yangtze River Navigation Centre

The Wuhan Yangtze River Navigation Centre (Fig. 4), currently being constructed in Wuhan, is a supertall building that consists of a 66-floor square main body and a triangular steel roof. This building will be 335 m tall after completion. The typical floor (Fig. 5) has a square size of 50.6 m × 50.6 m. The symmetric axis is 45° from the north. The inner tube has a square shape with a constant size of 28.2 m × 28.2 m. The outer frame tube consists of four concrete-filled-tube (CFT) columns at the corners and 16 square steel reinforced concrete (SRC) columns in the middle of each facade. The diameters of the four CFT columns and the widths of the 16 SRC columns decrease from 2.2 m at the bottom of the structure to 1.0 m at the top.

Fig. 4. Wuhan Yangtze River Navigation Centre

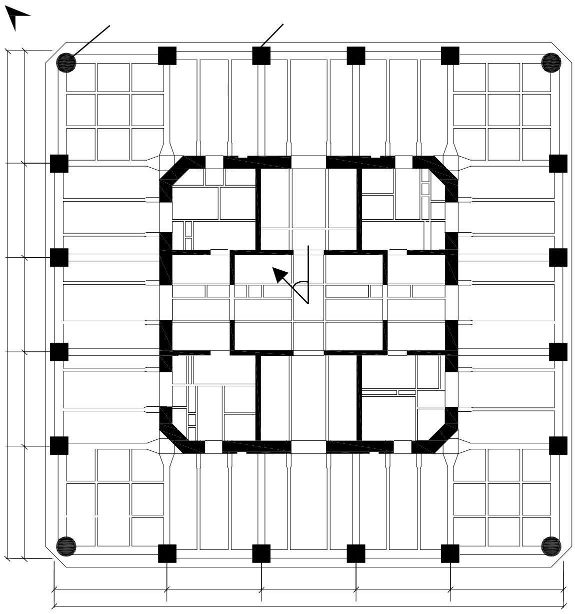

Fig. 5. A typical floor of Wuhan Yangtze River Navigation Centre

3.2. SHM system of the structure

An SHM system is installed on the skyscraper to monitor the structural performance during construction and service stages. Six monitoring sections are established at the storeys of 10, 18, 28, 38, 48 and 58, which correspond to heights of 47.05, 83.05, 129.55, 176.05, 222.55 and 265.05 m, respectively.

Fig. 6 shows the sensor layout of a typical monitoring section, which consists of 32 vibrating wire strain gauges and 8 temperature sensors. All strain gauges are distributed in east, south, west and north zones. For example, in the east zone, one strain gauge is installed in the CFT column, named S-E1 (‘S’ represents ‘strain,’ and ‘E’ is for ‘east’), four in the SRC columns (named S-E2 – S-E5), one in the core wall (S-E6) and two in the beams (named S-E7 and S-E8). The vibrating wire strain gauges can measure the strain and temperature at the same point. The temperature sensors are installed in the eight middle SRC columns, denoted as T-A1 and T-A2 to T-D1 and T-D2. All strain gauges and temperature sensors are embedded in the concrete 60 mm from the surface. The sampling rate of the strain gauges and temperature sensors is 10 min per reading.

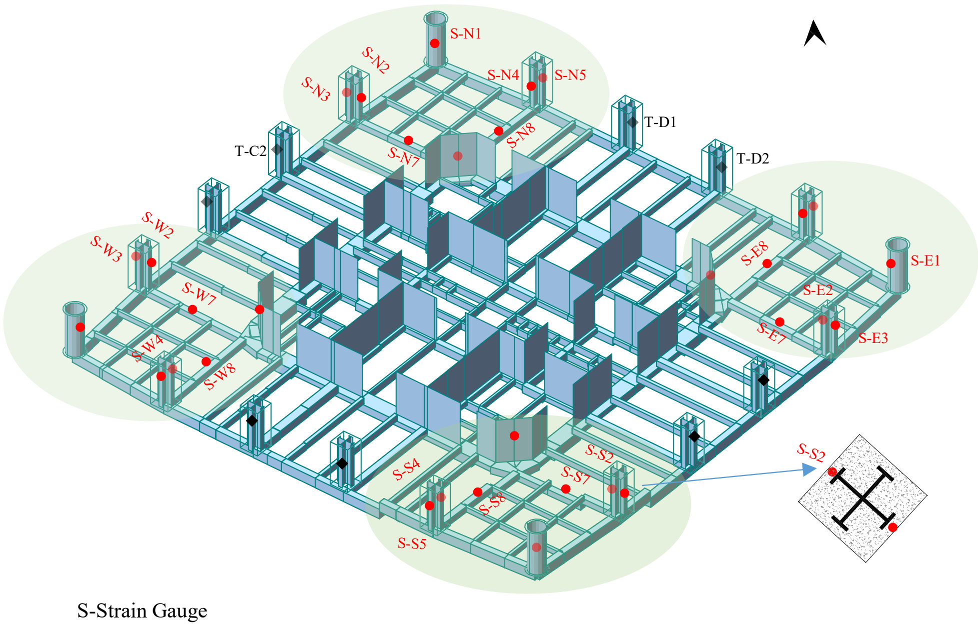

Fig. 6. Sensor layout of a typical monitoring section

4. 3D FE model of the supertall building

4.1. Establishment of the FE model

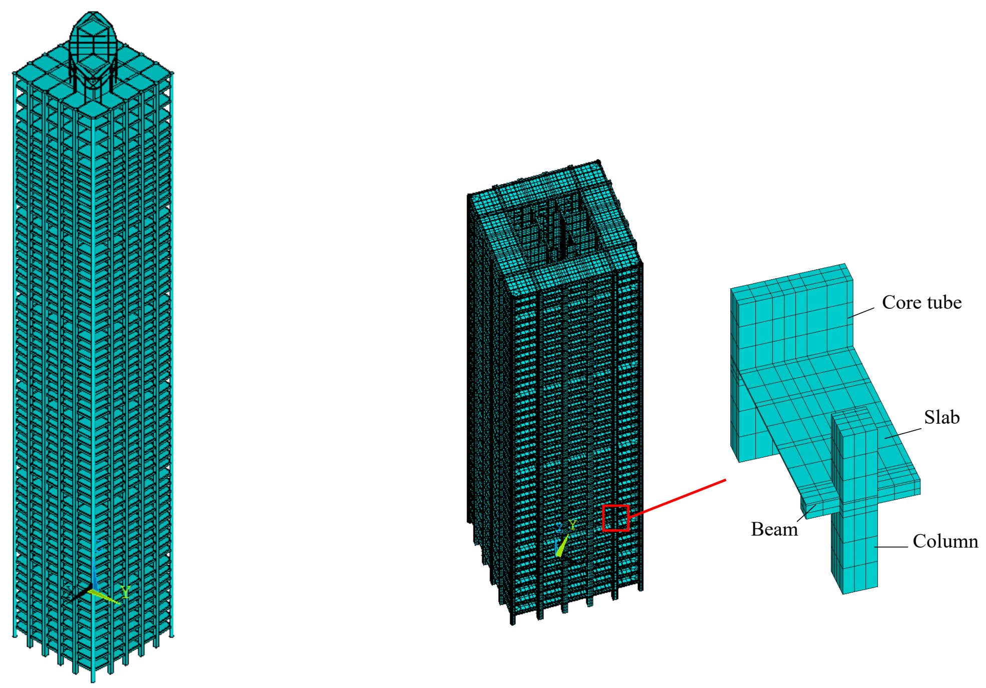

(a) FE model of the entire structure

(b) 42-floor FE model in one construction stage (195 m)

Fig. 7. FE model of Wuhan Yangtze River Navigation Centre

The FE model is established on the platform ANSYS. During the heat transfer analysis, the element type Solid90 is used for all elements, each consisting of 20 nodes with one thermal DOF at each node. The FE model is established according to the actual geometry of the structure, as shown in Fig. 7(a). The structure model mainly consists of four components, namely, the columns, wall, beams and slabs. All components are segmented into regular shapes to facilitate the use of the hexahedron mesh, as shown in Fig. 7(b). Different mesh sizes are adopted for different components to compromise the computational accuracy and efficiency. Fig. 8 shows that the columns and the walls are vertically divided into six parts per floor. The minimum element sizes of the columns and the walls are 0.12 m in vertical. The beams are divided by the slabs into two parts: the upper parts have the same thickness as the slabs, and the remaining parts have an element size of 0.48 m. A rough mesh size of 0.6 m is adopted for the slabs, given its insensitivity to temperature change. In the present study, we investigate one construction stage of the structure that is 42 story 195 m tall. The corresponding FE model contains 2,293,764 nodes and 404,763 elements.

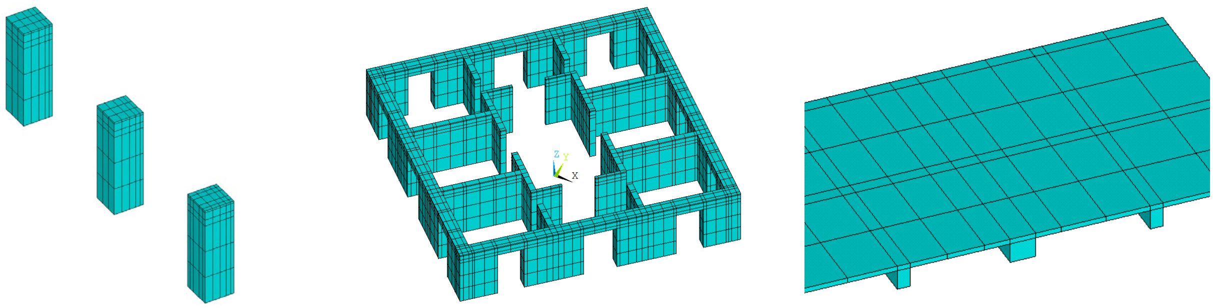

(a) Columns (b) Walls (c) Beams and slabs

Fig. 8. FE meshes of different components

4.2. Determination of the irradiation and shade elements

After completing the FE model, a virtual sun is established, which is simulated as a flat cuboid. The positions of the virtual sun are determined according to Eqs. (7) and (8). The size of the virtual sun element (S_1) and virtual sun-structure distance (S_2) have a significant effect on the number of the selected irradiation elements They are determined by maximizing the irradiation elements. When S_1 is considerably large, the virtual sun–structure radiation pairs cannot meet the requirements of parallel light, thereby resulting in inaccurate determination of the irradiation elements; when S_1 is considerably small, the angle coefficients between the virtual sun element and the structural elements are nearly equal to 0, thereby resulting in a small number of irradiation elements. Fig. 9(a) shows that the number of the selected irradiation elements reaches the maximum when S_1 =0.5 m. The size of the virtual sun element is finally set as 0.5 m × 0.5 m × 0.05 m. Similarly, Fig. 9(b) shows that the maximum number of irradiation elements is achieved as S_2 = 500 m. The angle coefficients between the virtual sun and the structural elements are calculated by the hemicube method. Afterwards, the irradiation and shade faces are determined according to the angle coefficient value. Fig. 10 shows the irradiation elements selected by the hemicube method at 9:00 and 12:00 on 27 July 2018. The irradiation elements vary as the sun's position changes.

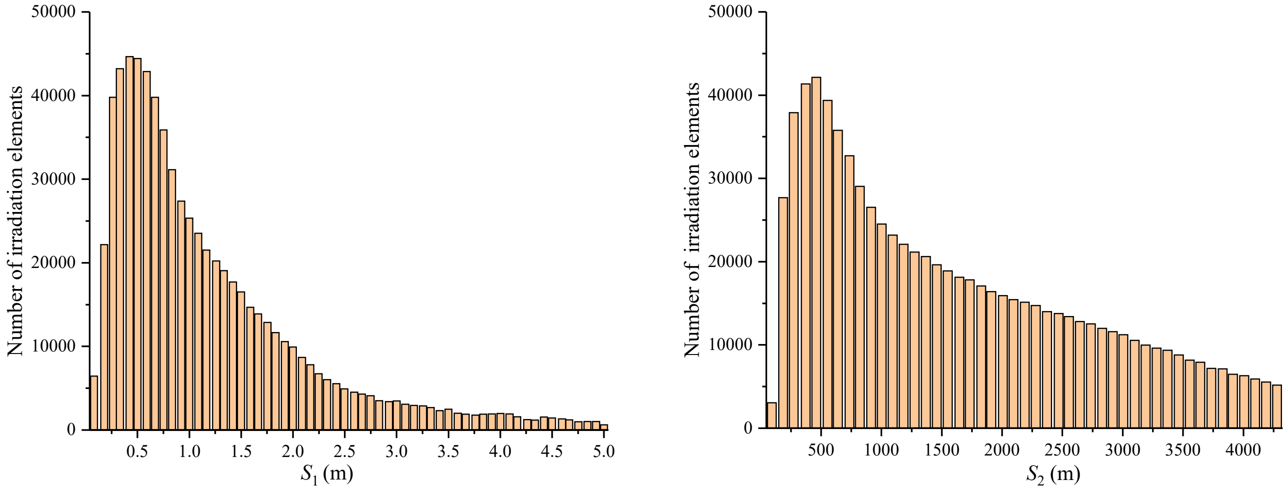

(a) Effects of the size of the virtual sun element (S_1)

(b) Effects of the virtual sun-structure distance (S_2)

Fig. 9. Factors that affect the number of irradiation elements

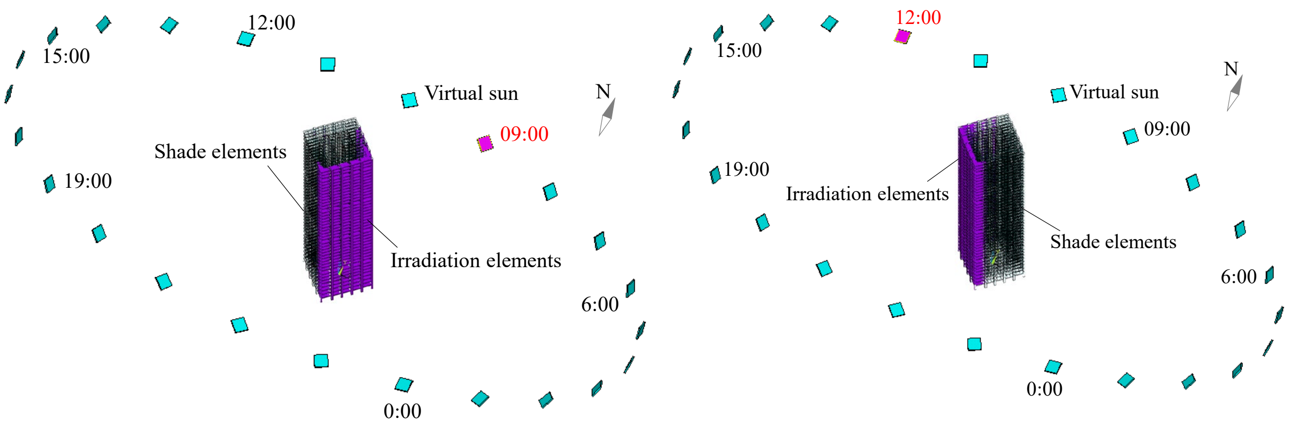

(a) At 9:00

(b) At 12:00

Fig. 10. Determination of irradiation and shade elements

4.3. Meteorological data and material parameters

The meteorological parameters on 27 July 2018 (Table 1) recorded from the meteorological monitoring station and the material properties (Table 2) are used for the transient heat transfer analysis.

The initial time is set as 0:00. Before calculating the temperature distribution on 27 July 2018, the initial thermal condition is determined via a pre-calculation [23] as follows: (i) The initial temperature distribution of the structure in the previous day (26 July 2018) is assigned as uniform; (ii) The thermal boundary condition on 26 July 2018 is applied to the FE model; and (iii) The heat transfer analysis is conducted, and the temperature distribution at different hours on 26 July 2018 is calculated. The temperature distribution at the end of 26 July 2018 is then assumed as steady and set as the initial temperature distribution of the structure on 27 July 2018. When applying the thermal boundary conditions, the meteorological parameters vary along the vertical direction, as shown in Fig. 11: 1) The mean wind speed varies exponentially with height, which is calculated as $v_h = v_0(h/h_0)^{0.28}$ (v_h and v_0 denote the mean wind speed at height h and h_0, respectively), according to the Chinese Design Specification [24]. 2) Air temperature decreases by 0.67 °C per 100 m along the height [14]. Solar radiation is not correlated to the height and thus regarded constant for the irradiation elements. The above parameters are input into ANSYS and the temperature distribution of the structure in each hour of the day is then calculated through the heat transfer analysis.

Table 1. Meteorological data measured on 27 July 2018

Time	0:00	1:00	2:00	3:00	4:00	5:00	6:00	7:00
Air temperature (°C)	34.4	34.3	34.1	32.1	32.4	31.6	31.5	31.8
Mean wind speed (m/s)	1.2	0.0	0.0	1.4	0.1	0.6	0.8	0.7
Solar radiation intensity (W/m^2)	0.0	0.0	0.0	0.0	0.0	0.0	126	282.8
Time	8:00	9:00	10:00	11:00	12:00	13:00	14:00	15:00
Air temperature (°C)	31.4	31.8	33.4	34.1	34.6	34.8	34.9	35.0
Mean wind speed (m/s)	2.2	2.7	2.6	2.5	4.0	3.2	2.9	3.7
Solar radiation intensity (W/m^2)	354.2	398.3	427.7	450.8	461.3	461.3	450.8	427.7
Time	16:00	17:00	18:00	19:00	20:00	21:00	22:00	23:00
Air temperature (°C)	33.7	32.2	32.1	31.2	30.7	30.0	29.9	29.5
Mean wind speed (m/s)	1.6	2.9	2.7	0.7	3.4	1.7	2.5	0.7
Solar radiation intensity (W/m^2)	397.6	352.8	277.2	123.2	0	0	0	0

Table 2. Concrete properties used in the FE model

Density (kg/m^3)	Elastic modulus (N/m^2)	Poisson's ratio	Coefficient of linear expansion ($°C^{-1}$)	Thermal conductivity ($W/(m°C)$)	Specific heat coefficient ($J/(kg°C)$)
2635.00	3.70×10^{10}	0.28	10.00×10^{-6}	2.33	921.00

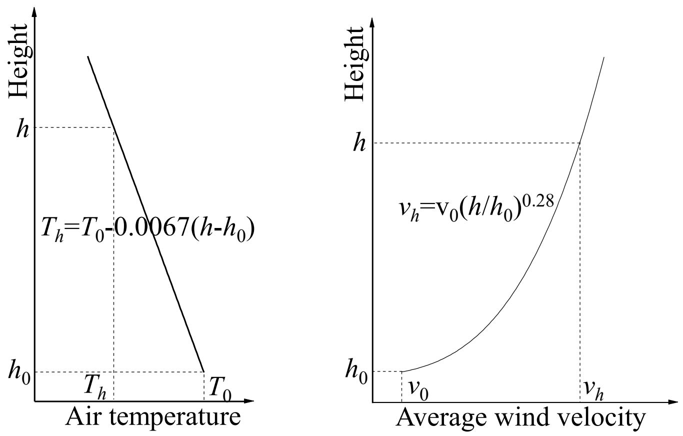

Fig. 11. Meteorological parameters in vertical direction

5. Temperature distribution and temperature-induced structural responses

5.1. Temperature distribution of the structure

Fig. 12 shows the calculated temperature distribution of the structure every two hours in the day. The temperatures of columns in the east facade start rising at 8:00. As the sun moves from the east to the west, the temperatures of the south and west facades rise gradually. The temperature on the irradiation face is significantly higher than that on the shade face. The maximum temperature of the model occurs at approximately 12:00. The high- and low-temperature zones change over time, and exhibit a nonuniform temperature distribution of the structure.

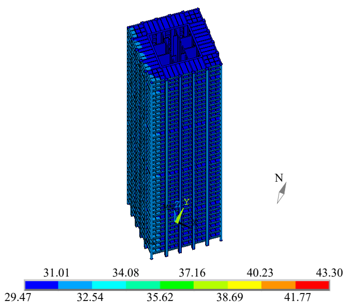

(a) 0:00

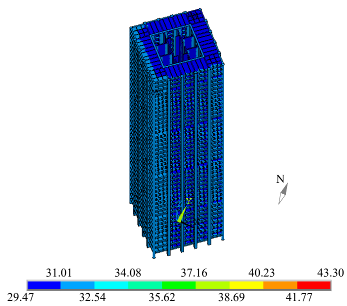

(b) 2:00

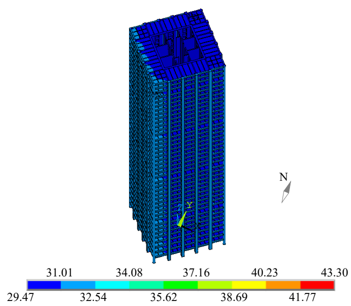

(c) 4:00

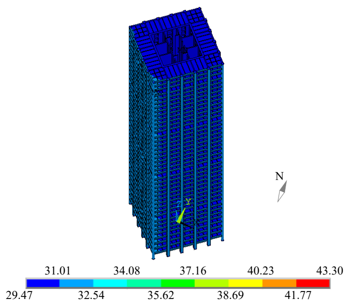

(d) 6:00

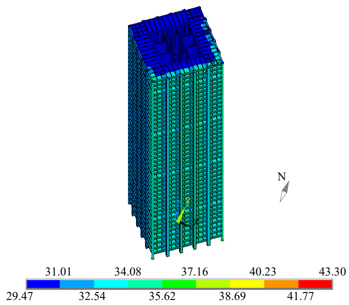

(e) 8:00

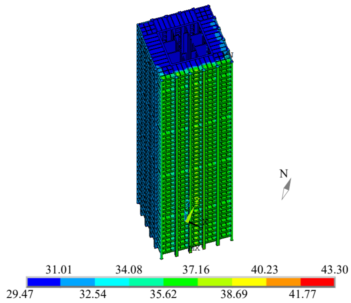

(f) 10:00

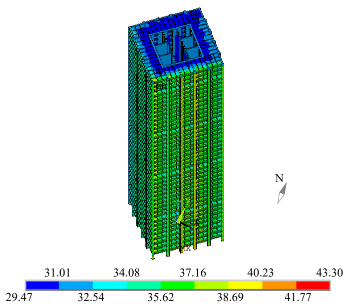

(g) 12:00

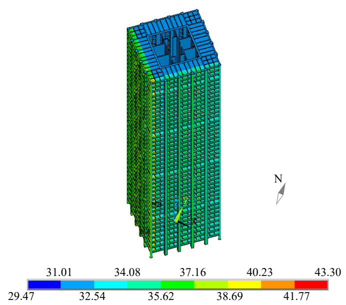

(h) 14:00

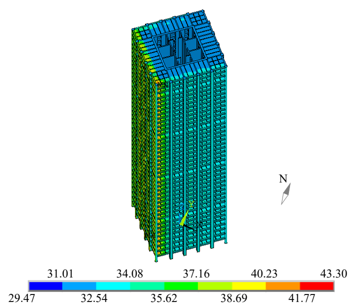

(i) 16:00

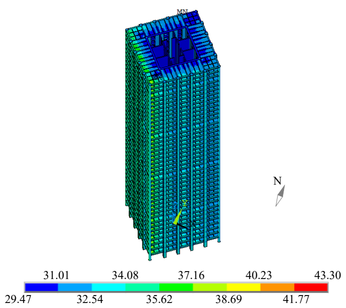

(j) 18:00

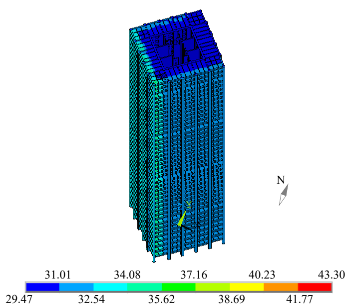

(k) 20:00

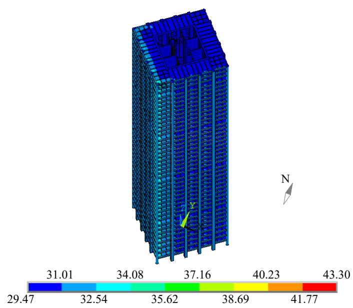

(l) 22:00

Fig. 12. Variation in temperature distribution of the structure on 27 July 2018

The calculated temperature distribution is compared with the field measurement data. At this construction stage, the measurement data of the 10th, 18th and 28th floors are available. The sensors S10-S2 ('10' means the 10th floor), S18-N3, S18-W3, S28-S3 and S28-N5 at different heights and directions are selected to investigate the temperature variations. Fig. 13 shows that the temperature at these five points starts rising at about 8:00. Point at the south facade (S28-S3) receives greater solar radiation intensity and the temperature is higher than other facades. S28-S3 reaches the maximum temperature at 12:00 and then decreases afterwards. Temperature at points S18-W3 and S18-N3 reach the maximum at 15:00, nearly 3 h later than the south (S28-S3). The variation of temperature in the inner column (T10-S2) is significantly smaller than that of the outer column (S28-S3). It can be seen from Fig. 13 that all calculated temperature results are in good agreement with the measured values in trend. The two sets of data are compared in Table 3. The maximum difference is less than 0.4 °C, which demonstrates that the proposed FE model and analysis simulate the structural temperature distribution accurately.

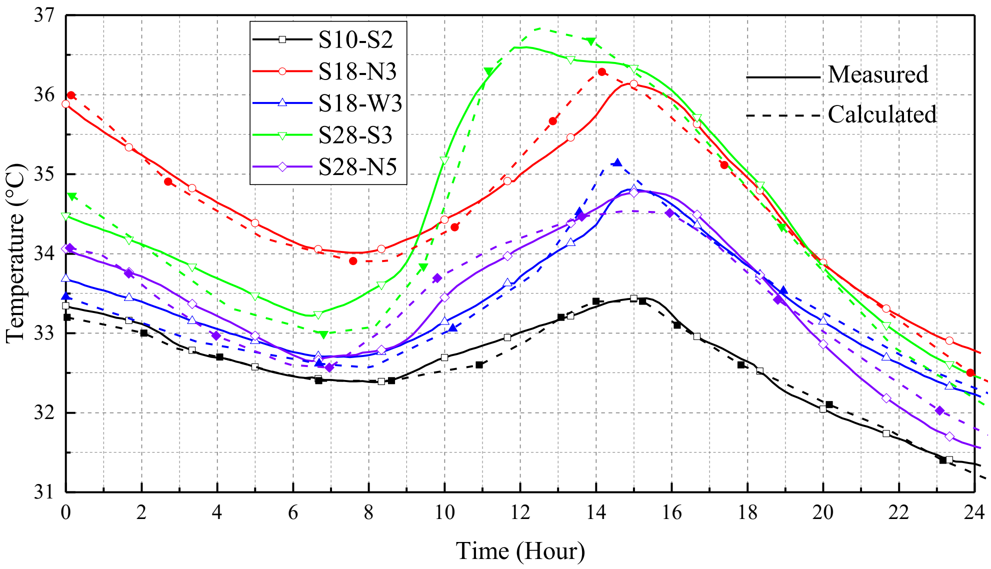

Fig. 13. Comparison of measured and calculated temperatures in one day

Table 3. Comparison of the measured and calculated temperature values

Points	Maximum temperature			Minimum temperature		
	Measured / °C	Calculated /°C	Absolute Error /°C	Measured / °C	Calculated /°C	Absolute Error /°C
S10-S2	33.44	33.40	0.04	31.36	31.25	0.11
S18-N3	36.31	36.15	0.16	32.80	32.47	0.33
S18-W3	34.83	35.21	0.38	32.27	32.35	0.08
S28-S3	36.61	36.85	0.24	32.46	32.21	0.25
S28-N5	34.79	34.54	0.25	31.58	31.81	0.23

For further verifying the reliability of the proposed technique in calculating the temperature distribution, the next three sunny days are selected. Fig. 14 shows the temperature variations of the five points from 28 July 2018 to 30 July 2018. The maximum difference between the calculated and measured temperatures is less than 0.7 °C, which also shows good agreement.

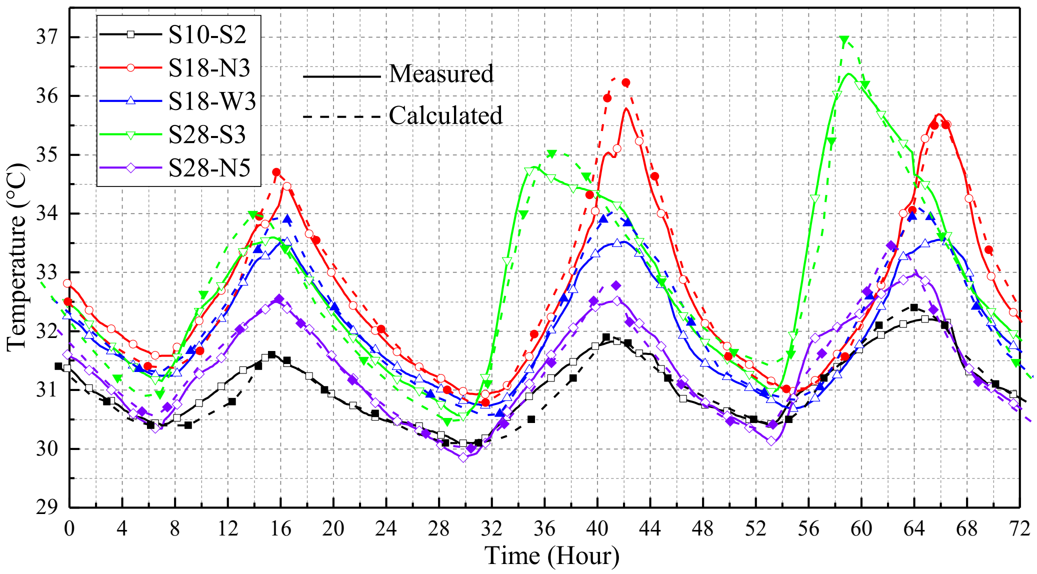

Fig. 14. Measured and calculated temperatures from 28 July 2018 to 30 July 2018

5.2. Temperature-induced structural responses

In addition to the temperature calculation, the FE model can be used to calculate the temperature-induced stresses and displacement. The obtained temperature data are applied to the structure model, which has the same mesh as the heat transfer analysis but with all elements being converted from type Solid90 to Solid186. Solid186 has also 20 nodes, and each node has three translational DOFs. The temperature-induced responses of the structure are calculated from the FE model without establishing a new FE model. This feature is a significant benefit of the present technique, given that establishing a new FE model and applying the temperature load are time consuming and need significant manual intervention.

The reinforcement is not considered in the FE model and the equivalent concrete elastic modulus is used to consider the reinforcement by the following equation:

$$E_{eq} = \frac{E_c A_c + E_s A_s}{A_c + A_s}, \tag{12}$$

where E_c is the elastic modulus of the concrete, E_s is the elastic modulus of the steel, A_c represents the area of the concrete and A_s represents the area of the steel.

With structural analysis, the temperature-induced stress at any point of the structure can be directly obtained. The calculated stresses are then compared with the field monitoring strain data. For axial loaded members, such as the columns, the field monitoring strain data are converted into the stress according to the following equation:

$$\sigma = E_{eq}(\varepsilon - \alpha_T \Delta T), \tag{13}$$

where σ is the stress, ε represents the total strain, α_T =10.0 × 10^{-6} $\mu\varepsilon$/°C is the linear expansion coefficient of concrete, and ΔT denotes the temperature change. Here only the vertical stress is discussed.

On 27 July 2018, the construction activity of the structure was minor. Thus, the influence of the construction load on the structural strain and stress can be ignored. Moreover, the shrinkage and creep of concrete are negligible within the short period of a day. The changes in structural strain and stress are mainly due to the temperature changes. Setting 0:00 as the reference, the changes in the stress in this day relative to the initial values are analysed and shown in Fig. 15. The stresses at these five points decreased (or compression became larger) as the temperature increased. The measured stress variations at point S28-S3, S18-N3, S18-W3, S28-N5 and S10-S2 are 1.3, 1.1, 1.0, 0.8 and 0.6 MPa, respectively. Compared to the temperature variations in Fig. 13, the stress variation of each point is positively correlated with its temperature variation. The calculated and measured stress variations have similar trends and their difference is small except one point of 0.39 MPa, as shown in Table 4. The stress variations in the next three days are also shown in Fig. 16. The maximum daily stress variation is approximately 2.0 MPa (at S28-S3) and the maximum difference is less than 0.5 MPa. The simplification of the reinforcement and nonhomogeneity of structural material properties may cause errors in the simulation results. On the other hand, the field measurement is also subject to errors.

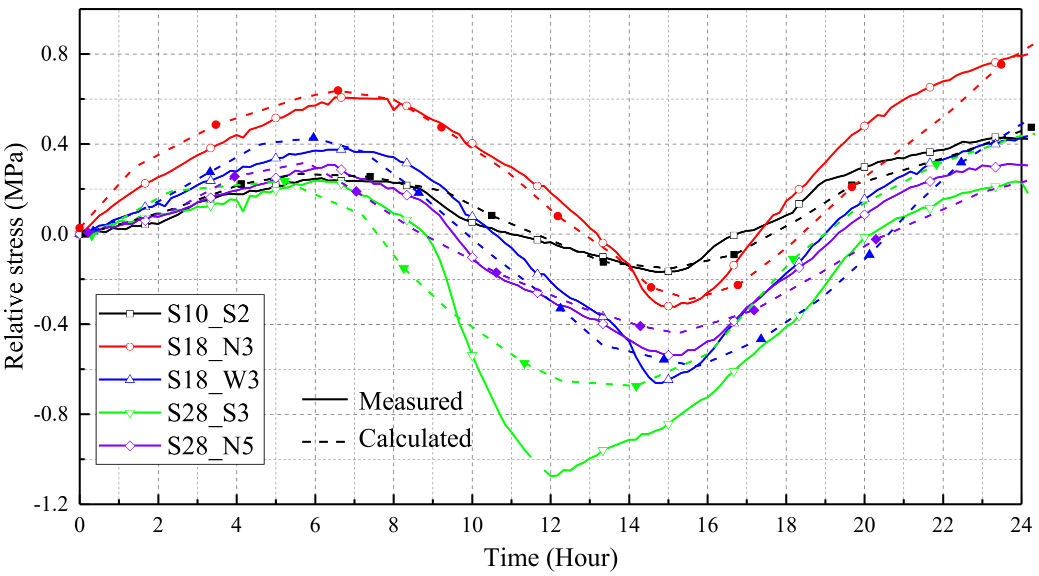

Fig. 15. Variation in vertical stresses on 27 July 2018

Table 4. Measured and calculated vertical stresses on 27 July 2018

Points	Maximum compressive stresses			Maximum tensile stresses		
	Measured /MPa	Calculated /MPa	Absolute Error /MPa	Measured /MPa	Calculated /MPa	Absolute Error /MPa

S10-S2	-0.17	−0.15	0.02	0.42	0.46	0.04
S18-N3	−0.33	−0.28	0.05	0.78	0.80	0.02
S18-W3	−0.66	−0.59	0.07	0.41	0.48	0.07
S28-S3	−1.07	−0.68	0.39	0.23	0.44	0.21
S28-N5	−0.55	−0.44	0.11	0.31	0.23	0.08

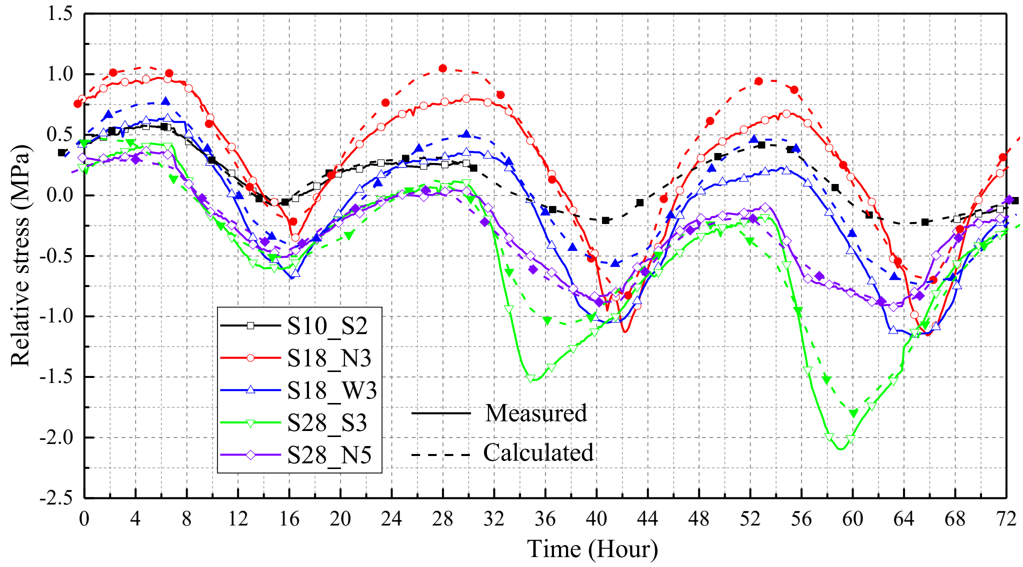

Fig. 16. Measured and calculated stress variations from 28 July 2018 to 30 July 2018

The temperature-induced horizontal displacement of the structure is also calculated. Twenty columns are symmetrically distributed around the structure, and their displacement represents the overall movement of the structure. The east–west and north–south displacements at the top of 20 columns are extracted from the calculation and then averaged. Fig. 17 shows the trajectory of the structure top on 27 July 2018 using the position at 0:00 as the origin point. The structure top leaned to the west from 6:00 to 11:00. Afterwards, the top moved to the north and then back to the east after 14:00. In the evening, the structure returned to the origin as the temperature dropped. The horizontal displacement mainly occurred during the daytime and changed with the position of the sun. The maximum horizontal displacement at the structure top was approximately 11 mm at 12:00, when the temperature difference between the irradiation and shade faces reached the maximum. The horizontal displacement at the structure top may become larger when the structural height increases.

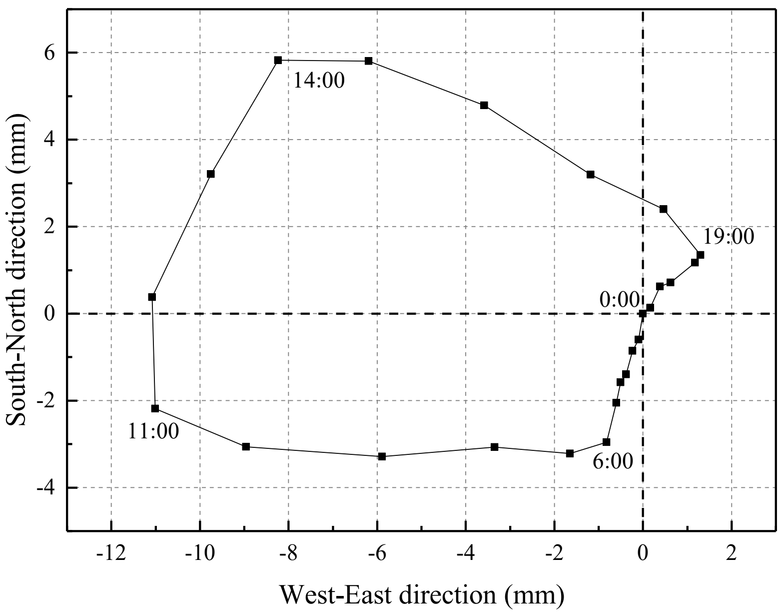

Fig. 17. Calculated horizontal displacement of the structure top on 27 July 2018

6. Conclusions

For supertall structures, the global heat transfer analysis is difficult to carry out because time- and space-varying thermal boundary conditions need to be applied manually. This study presents an efficient automatic approach to calculating the temperature distribution and temperature-induced response of supertall structures. The technique is successfully applied to Wuhan Yangtze River Navigation Centre, on which a long-term SHM system is being installed. Field measurement data are used to verify the calculated temperature and stress results. The following conclusions are drawn.

1. Introducing the radiation calendar system enables the determination of the relative position of the sun expediently. The virtual sun is used to distinguish the irradiation and shade faces of the structure.

2. In this study, the FE model for calculating the structure's temperature distribution does not need to select the boundary conditions manually. This FE model has good practicality and robustness for predicting the temperature distribution of structures at any time. The calculated temperature shows a good agreement with the field measurement data.

3. The calculated temperature distribution is transferred into the temperature load of the same FE model to estimate the stresses and displacement of the structure without establishing a new FE model. The calculated stresses agree well with the field measurement data.

Acknowledgements

This work is supported by grants from the National Natural Science Foundation of China (NSFC, Project No. 51629801), the Research Grants Council of the Hong Kong Special Administrative Region, China (Project No. PolyU 152621/16E) and the Fundamental Research Funds for the Central Universities (HUST: 2016JCTD113).

References

[1] Su JZ, Xia Y, Zhu LD, Zhu HP, Ni YQ. Typhoon-and temperature-induced quasi-static responses of a supertall structure. Engineering Structures. 2017;143:91-100.

[2] Zhou GD, Yi TH. Thermal load in large-scale bridges: a state-of-the-art review. International Journal of Distributed Sensor Networks. 2013;9(12):217983.

[3] Mirambell E, Aguado A. Temperature and stress distributions in concrete box girder bridges. Journal of Structural Engineering. 1990;116(9):2388-409.

[4] Hambly EC. Temperature distributions and stresses in concrete bridges. Structural Engineer. 1978;56 A(5):143-8.

[5] Tayşi N, Abid S. Temperature distributions and variations in concrete box-girder bridges: experimental and finite element parametric studies. Advances in Structural Engineering. 2015;18(4):469-86.

[6] Liu CY, Dewolf JT. Effect of temperature on modal variability of a curved concrete bridge under ambient loads. Journal of Structural Engineering. 2007;133(12):1742-51.

[7] Branco FA, Mendes PA. Thermal actions for concrete bridge design. Journal of Structural Engineering. 1993;119(8):2313-31.

[8] Liu HB, Chen ZH, Zhou T. Investigation on temperature distribution and thermal behavior of large span steel structures considering solar radiation. Advanced Steel Construction. 2013;9(1):41-58.

[9] Xia Q, Zhang J, Tian YD, Zhang YF. Experimental study of thermal effects on a long span suspension bridge. Journal of Bridge Engineering. 2017; 22(7): 0001083.

[10] Pirner M, Fischer O. Long-time observation of wind and temperature effects on TV towers.

Journal of Wind Engineering & Industrial Aerodynamics. 1999;79(1-2):1-9.

[11] Tamura Y, Matsui M, Pagnini LC, Ishibashi R, Yoshida A. Measurement of wind-induced response of buildings using RTK-GPS. Journal of Wind Engineering & Industrial Aerodynamics. 2002;90(12-15):1783-93.

[12] Breuer P, Chmielewski T, Górski P, Konopka E, Tarczyński L. The Stuttgart TV Tower — displacement of the top caused by the effects of sun and wind. Engineering Structures. 2008;30(10):2771-81.

[13] Xia Y, Zhang P, Ni YQ, Zhu HP. Deformation monitoring of a super-tall structure using real-time strain data. Engineering Structures. 2014;67:29-38.

[14] Su JZ, Xia Y, Ni YQ, Zhou LR, Su C. Field monitoring and numerical simulation of the thermal actions of a supertall structure. Structural Control & Health Monitoring. 2017;24(4):e1900.

[15] Hu YD, Hou R, Xia Q, Xia Y. Temperature-induced displacement of supertall structures: A case study. Advances in Structural Engineering. 2018:1369433218795288.

[16] Elbadry MM, Ghali A. Temperature variations in concrete bridges. Journal of Structural Engineering. 1983;109(10):2355-74.

[17] Hedegaard BD, French CEW, Shield CK. Investigation of thermal gradient effects in the I-35W St. Anthony Falls Bridge. Journal of Bridge Engineering. 2012;18(9):890-900.

[18] Larsson O, Thelandersson S. Estimating extreme values of thermal gradients in concrete structures. Materials & Structures. 2011;44(8):1491-500.

[19] Xia Y, Chen B, Zhou XQ, Xu YL. Field monitoring and numerical analysis of Tsing Ma Suspension Bridge temperature behavior. Structural Control & Health Monitoring.

2013;20(4):560-75.

[20] Guo MH, Wang ZF, Zhang JH, Sun FH, Zhang XL. Accurate altitude–azimuth tracking angle formulas for a heliostat with mirror–pivot offset and other fixed geometrical errors. Solar Energy. 2011;85(5):1091-100.

[21] Xu F, Wang B, Zhang HL. Improvement upon the formulas for solar position in analysis of sunlight distribution in buildings. Journal of Chongqing Jianzhu University. 2008;30(5):130-134. (in Chinese).

[22] Cohen MF, Greenberg DP. The hemi-cube: A radiosity solution for complex environments. ACM SIGGRAPH Computer Graphics. 1985;19(3):31-40.

[23] Zhou LR, Xia Y, Brownjohn JMW, Koo KY. Temperature analysis of a long-span suspension bridge based on field monitoring and numerical simulation. Journal of Bridge Engineering. 2016;21(1):04015027.

[24] JTG/T 3360-01-2018, Wind-resistent design specification for highway bridges. Ministry of Transport of the People's Republic of China, Beijing; 2018.